

# Experimental Realization of Universal Geometric Quantum Gates with Solid-State Spins

C. Zu<sup>1</sup>, W.-B. Wang<sup>1</sup>, L. He<sup>1</sup>, W.-G. Zhang<sup>1</sup>, C.-Y. Dai<sup>1</sup>, F. Wang<sup>1</sup>, L.-M. Duan<sup>1,2</sup>

<sup>1</sup>*Center for Quantum Information, IIIS, Tsinghua University, Beijing 100084, China*

<sup>2</sup>*Department of Physics, University of Michigan, Ann Arbor, Michigan 48109, USA*

PACS numbers:

Experimental realization of a universal set of quantum logic gates is the central requirement for implementation of a quantum computer. An all-geometric approach to quantum computation [1, 2] offered a paradigm for implementation where all the quantum gates are achieved based on the Berry phases [3] and their non-abelian extensions, the holonomies [4], from geometric transformation of quantum states in the Hilbert space [5]. Apart from its fundamental interest and rich mathematical structure, the geometric approach has some built-in noise-resilient features [1, 2, 6, 7]. On the experimental side, geometric phases and holonomies have been observed using nuclear magnetic resonance with thermal ensembles of liquid molecules [8, 9], however, such systems are known to be non-scalable for quantum computing [10]. There are proposals to implement geometric quantum computation in scalable experimental platforms such as trapped ions [11], superconducting qubits [12], or quantum dots [13], and a recent experiment has realized geometric single-bit gates with the superconducting system [14]. Here, we report the first experimental realization of a universal set of geometric quantum gates with solid-state spins of the diamond defects. The diamond defects provide a scalable experimental platform [15–17] with the potential for room-temperature quantum computing [16–19], which has attracted strong interest in recent years [20]. Based on advance of coherent control in this system [15–20], our experiment shows that all-geometric and potentially robust quantum computation can be realized with solid-state spin qubits.

Under adiabatic cyclic evolution, a non-degenerate eigenstate of a quantum system acquires a phase factor, which has a dynamical component proportional to the time integral of the eigenenergy and a geometric component determined by the global property of the evolution path. This geometric phase, first discovered by Berry [3], has found connection with many important physics phenomena [21]. If the system has degenerate eigenstates, the Berry's phase is replaced by an geometric unitary operator acting on the degenerate subspace, termed as holonomy from the differential geometry.

The holonomies are in general non-commutable with each other. In the proposal of geometric quantum computation [1, 2], such holonomies are exploited to realize a universal set of quantum gates, compositions of which then can fulfill arbitrary quantum computation tasks. As holonomies are determined by global geometric properties, geometric computation is more robust to certain control errors [1, 2, 6, 7]. Implementation of geometric quantum computation has been proposed in several qubit systems [11–13], however, it remains experimentally challenging to realize a universal set of gates all by holonomies, because of the requirements of slow adiabatic evolution and a complicated level structure.

In the recent proposal of non-adiabatic geometric quantum computation [6, 22], universal quantum gates are constructed fully by geometric means without requirement of the adiabatic condition, thereby combining speed with universality. Under a cyclic evolution of the system Hamiltonian  $H(t)$  (with  $H(\tau) = H(0)$ ), let  $|\xi_l(t)\rangle$  ( $l = 1, 2, \dots, M$ ) denote instantaneous orthonormal bases (moving frames) which coincide with the basisvectors  $|\xi_l\rangle$  of the computational space  $C$  at  $t = 0, \tau$  with  $|\xi_l(\tau)\rangle = |\xi_l(0)\rangle = |\xi_l\rangle$ . The evolution operator  $U(\tau)$  on the basis states  $|\xi_l\rangle$  has two contributions: a dynamic part and a fully geometric part [6]. If the parallel-transport condition  $\langle \xi_l(t) | H(t) | \xi_{l'}(t) \rangle = 0$  is satisfied for any  $l, l'$  at any time  $t$ , the dynamic contribution becomes identically zero, and  $U(\tau)$  is given by

$$U(\tau) = T \exp \left[ i \int_0^\tau A dt \right], \quad (1)$$

where  $T$  denotes the time-ordered integration and  $A = [A_{ll'}] = [\langle \xi_l(t) | i\partial_t | \xi_{l'}(t) \rangle]$  represents the  $M \times M$  connection matrix [6]. The form of  $U(\tau)$  is identical to the Wilczek-Zee holonomy in the adiabatic case [4, 6].

Our experiment realizes a universal set of quantum gates all by use of the nonadiabatic holonomies [6]. Single-bit gates, together with entangling controlled-NOT (CNOT) operation, are universal for quantum computation. Our realization is based on control of electron and nuclear spins in a diamond nitrogen-vacancy (NV) center that form effectively a quantum register [20]. To realize the single-bit geometric gates, we manipulate the electron spin states of a NV center (Fig. 1a) in a synthetic diamond at room temperature (see Methods for

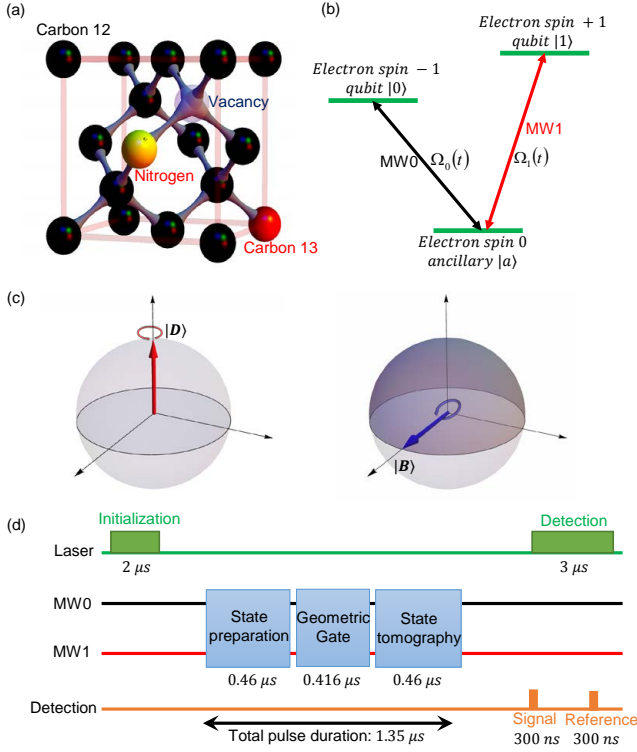


FIG. 1: **Geometric gates in a diamond nitrogen vacancy center.** **a**, Illustration of a nitrogen vacancy (NV) center in a diamond with a proximal  $C^{13}$  atom. **b**, Encoding of a qubit in the spin-triplet ground state of the NV center and the microwave coupling configuration. The electron spin 0 state provides an ancillary level  $|a\rangle$  for geometric manipulation of the qubit. **c**, A geometric picture of the holonomic gates. Under a cyclic Hamiltonian evolution, the dark  $|D\rangle$  (bright  $|B\rangle$ ) state rotates by  $2\pi$  along the north pole (equator) of the Bloch sphere, acquiring a geometric phase of 0 ( $\pi$ ) given as half of the swept solid angle. When we choose different forms of the dark and bright states by controlling parameters in the Hamiltonian, this state-dependent geometric phase leads to the corresponding holonomic gates. **d**, The time sequence for implementation and verification of single-qubit geometric gates.

description of the experimental setup). The NV center has a spin-triplet ground state. We take the Zeeman components  $|m = -1\rangle \equiv |0\rangle$  and  $|m = +1\rangle \equiv |1\rangle$  as the qubit basis states and use  $|m = 0\rangle \equiv |a\rangle$  as an ancillary level for geometric manipulation of the qubit. The spin state is initialized through optical pumping to the  $|m = 0\rangle$  level and read out by distinguishing different fluorescence levels of the states under illumination of a short green laser pulse [20] (see Methods for calibration of fluorescence levels of different states). We apply a magnetic field of 451 G along the NV axis using a permanent magnet. Under this field, the nearby nuclear spins are polarized by optical pumping [23], enhancing the coherence time of the electron spin.

The transitions from the qubit states  $|0\rangle, |1\rangle$  to the

ancillary level  $|a\rangle$  are coupled by microwave pulses controlled through an arbitrary waveform generator (AWG), with Rabi frequencies  $\Omega_0(t)$ ,  $\Omega_1(t)$ , respectively (Fig. 1b). We vary the amplitude  $\Omega(t) = \sqrt{\Omega_0^2 + \Omega_1^2}$  but fix the ratio  $\Omega_1/\Omega_0 = e^{i\varphi} \tan \theta$  to be constant. The Hamiltonian for the coupling between these three levels takes the form

$$H_1(t) = \hbar \Omega(t) [(\cos \theta |0\rangle + e^{i\varphi} \sin \theta |1\rangle) \langle a| + H.c.] \quad (2)$$

where  $\hbar$  is the Planck constant divided by  $2\pi$  and  $H.c.$  denotes the Hermitian conjugate. Define the bright state as  $|B\rangle = \cos \theta |0\rangle + e^{i\varphi} \sin \theta |1\rangle$  and the dark state as  $|D\rangle = -e^{-i\varphi} \sin \theta |0\rangle + \cos \theta |1\rangle$ . When  $\Omega(t)$  makes a cyclic evolution with  $\Omega(0) = \Omega(\tau) = 0$ , the bright state evolves as  $|B(t)\rangle = e^{i\alpha(t)} [\cos \alpha(t) |B\rangle + \sin \alpha(t) |a\rangle]$ , where  $\alpha(t) \equiv \int_0^t \Omega(t') dt'$ , while the dark state remains unchanged. After a cyclic evolution with  $\alpha(\tau) = \pi$ , the bright (dark) state picks up a geometric phase of  $\pi$  (0), respectively, as illustrated in Fig. 1c. We take the moving frame as  $|\xi_0(t)\rangle = \cos \theta |B(t)\rangle - e^{i\varphi} \sin \theta |D\rangle$ ,  $|\xi_1(t)\rangle = e^{-i\varphi} \sin \theta |B(t)\rangle + \cos \theta |D\rangle$ , which makes a cyclic evolution with  $|\xi_l(0)\rangle = |\xi_l(\tau)\rangle = |l\rangle$  ( $l = 0, 1$ ). For this evolution, one can easily check that the condition  $\langle \xi_l(t) | H(t) | \xi_{l'}(t) \rangle = 0$  is always satisfied, so there is no dynamic contribution to the evolution operator  $U(\tau)$  [6]. Using the expression (1), we find the holonomy

$$U(\tau) = \begin{bmatrix} -\cos(2\theta) & -e^{i\varphi} \sin(2\theta) \\ -e^{-i\varphi} \sin(2\theta) & \cos(2\theta) \end{bmatrix} \quad (3)$$

under the computational basis  $\{|0\rangle, |1\rangle\}$ .

We evolve the Rabi frequencies  $\Omega_i(t)$  along three different loops, with the parameters  $(\theta, \varphi)$  chosen respectively as  $(3\pi/4, 0)$ ,  $(3\pi/4, \pi/8)$ ,  $(5\pi/8, 0)$ . The three geometric gates resulting from these cyclic evolutions are denoted by the NOT gate  $N$ , the rotation gate  $A$ , and the Hadamard gate  $H$ , respectively. The combination of the gates  $N$  and  $A$  gives the well-known  $\pi/8$ -gate  $T = NA$ , which, together with the Hadamard gate  $H$ , make a universal set of single-bit gates. To characterize these geometric gates, we use quantum process tomography by preparing and measuring the qubit in different bases [25], with the time sequence shown in Fig. 1d. The matrix elements for each process are shown in Fig. 2a-2c, which are compared with the corresponding elements of the ideal gates. From the process tomography (see Methods), we find the process fidelity  $F_P = (96.5 \pm 1.9)\%$ ,  $(96.9 \pm 1.5)\%$ ,  $(92.1 \pm 1.8)\%$  respectively for the  $N$ ,  $A$ , and  $H$  gates. The major contribution to the infidelity actually comes from the state preparation and detection error in quantum process tomography. To measure the intrinsic gate error, we concatenate a series of gates and examine the fidelity decay as the number of gates increases [19]. As an example, we show in Fig. 2d the fidelity decay by concatenating the NOT gates. From the data, we find the intrinsic error per gate is about

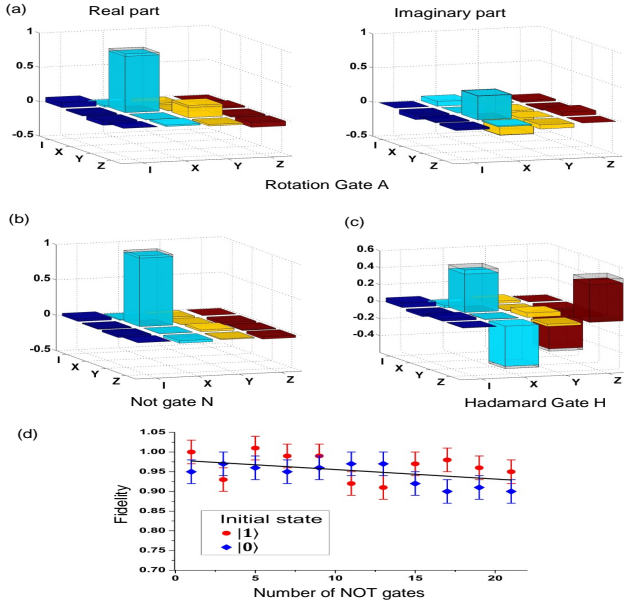


FIG. 2: **Experimental results for single-bit geometric gates.** The measured process matrix elements for the rotation gate  $A$  (a), the NOT gate  $N$  (b), and the Hadamard gate  $H$  (c). The measured tiny imaginary parts of the process matrices for the NOT and the Hadamard gates are not shown. The hollow caps in these figures denote the corresponding matrix elements for the ideal gates. d, The measured fidelities of the final states compared with the ideal output (error bars denote s.d.) after application of a sequence of the geometric NOT gates, with the initial state taken as  $|0\rangle$  and  $|1\rangle$ , respectively. By fitting the data under the assumption of independent error for each gate, we obtain the error induced by each NOT gate at  $(0.24 \pm 0.06)\%$ .

0.24%. This can be compared with the 1% error rate for the dynamic NOT gate using optimized pulses by the same method of measurement [19]. The achieved high fidelity indicates that the geometric manipulation is indeed resilient to control errors.

To realize the geometric quantum CNOT gate, we use one nearby  $C^{13}$  nuclear spin as the control qubit (with the basisvectors  $|\uparrow\rangle, |\downarrow\rangle$ ) and the NV center electron spin as the target qubit [24]. Both the electron spin and the nuclear spin are polarized through optical pumping under the 451 G magnetic field, which is confirmed by the optically detected magnetic resonance (ODMR) spectroscopy shown in Fig. 3b. The spins are interacting with each other through hyperfine and dipole couplings, and the resultant level configuration is shown in Fig. 3a. By applying state-selective microwave (MW) and radio-frequency (RF) pulses, we can couple different levels. In particular, with the MW0 and MW1 pulses with Rabi frequencies  $\Omega_0(t)$ ,  $\Omega_1(t)$ , we have the following coupling Hamiltonian

$$H_2(t) = \hbar\Omega(t)[(|0, \uparrow\rangle - |1, \uparrow\rangle)\langle a, \uparrow| + H.c.]/\sqrt{2}, \quad (4)$$

where we have fixed the ratio  $\Omega_1/\Omega_0 = -1$ . Under a

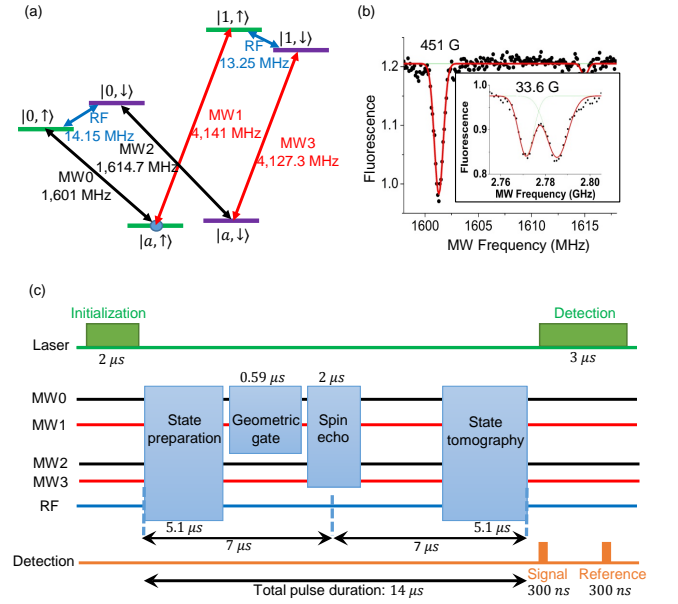


FIG. 3: **Level scheme and pulse sequence for the geometric CNOT gate.** a, The level structure of the electron and the nuclear spins for the geometric CNOT gate and the microwaves and RF coupling configuration. b, Optically detected magnetic resonance (ODMR) spectroscopy by measuring the fluorescence level while scanning the frequency of the microwave that couples to the electron spin 0 to 1 transition. The two dips at 33.6 G magnetic field (shown in the insert) represent the hyperfine splitting caused by the unpolarized nuclear spin. The very asymmetric dips at 451 G field indicates that the nuclear spin has been polarized. c, The time sequence for implementation and verification of the geometric CNOT gate between the electron and the nuclear spins. The CNOT gate is implemented by applying MW0 and MW1 pulses simultaneously. The other microwaves (MW0, MW1, MW2, and MW3) are used for implementation of a spin echo to increase the spin coherence time. To verify the CNOT gate, we use a combination of the microwave and the RF pulses to prepare various initial superposition states and measure the final output in different bases through quantum state tomography.

cyclic evolution of  $\Omega(t)$  with  $\int_0^\tau \Omega(t) dt = \pi$ , we find the holonomy  $U(\tau) = |\uparrow\rangle\langle\uparrow| \otimes N + |\downarrow\rangle\langle\downarrow| \otimes I$  using the formula (1), where  $I$  denotes the  $2 \times 2$  unit matrix. This achieves exactly the quantum CNOT gate.

To characterize the geometric CNOT gate, we apply the gate to the qubit basis states as well as their superpositions, and measure the fidelity of the final states compared with the ideal outputs through the quantum state tomography [25]. The superposition of the nuclear spin states required for state preparation and measurement is generated through RF pulses, which take longer times compared with the microwave pulses due to the much smaller magnetic moment of the nuclear spin. The electron spin decoherence is significant during the slow RF pulses. To correct that, we apply a Hahn spin echo in the middle of the whole operation

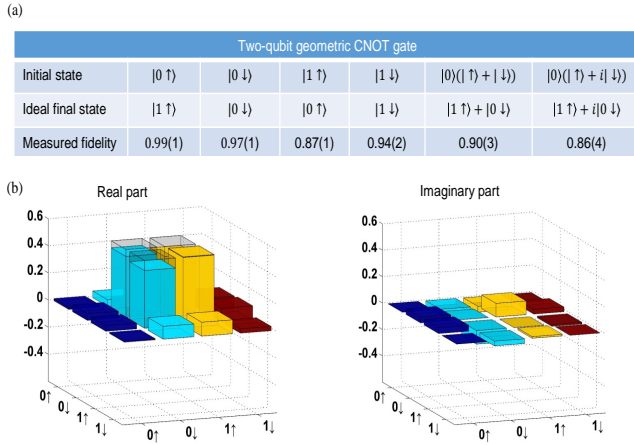


FIG. 4: **Experimental results for the geometric CNOT gate.** **a**, Measured output state fidelities of the geometric CNOT gate under a few typical input states, where the number in the bracket represents the error bar (s.d.) in the last digit. **b**, The matrix elements of the output density operator reconstructed through quantum state tomography when the geometric CNOT is applied to the product state  $|0\rangle(|\uparrow\rangle + |\downarrow\rangle)/\sqrt{2}$ . The hollow caps denote the matrix elements for the ideal output state under a perfect gate.

with the time sequence shown in Fig. 3c. The measured state fidelities are listed in Fig. 4a under typical input states. As a hallmark of the entangling operation, the geometric CNOT gate generates entanglement from the initial product state. As an example, for the input state  $|0\rangle \otimes (|\uparrow\rangle + |\downarrow\rangle)$  (unnormalized), the matrix elements of the output density operator are shown in Fig. 4b, with a measured entanglement fidelity of  $(90.2 \pm 2.5)\%$  and concurrence of  $0.85 \pm 0.05$ , which unambiguously confirms entanglement [10].

Our experimental realization of a universal set of holonomic gates with individual spins paves the way for all-geometric quantum computation in a solid-state system. The electron and nuclear spins of different NV centers can be wired up quantum mechanically to form a scalable network of qubits through, e.g., the direct dipole interaction [16, 18], the spin-chain assisted coupling by the nitrogen dopants [17, 26], or the photon-mediated coupling [15, 27, 28]. The technique employed here for geometric realization of universal gates may also find applications in other scalable experimental systems, such as trapped ions or superconducting qubits. The geometric phase is closely related to the topological phase [29, 30], and the demonstration of gates all by holonomies is an important step towards realization of topological computation [30], the most robust way of quantum computing.

- [1] Zanardi, P. & Rasetti, M. Holonomic quantum computation. Phys. Lett. A 264, 94–99 (1999).
- [2] Pachos, J., Zanardi, P. & Rasetti, M. Non-Abelian Berry connections for quantum computation. Phys. Rev. A 61, 010305(R) (2000).
- [3] Berry, M. V. Quantal phase-factors accompanying adiabatic changes. Proc. R. Soc. Lond. A 392, 45–57 (1984).
- [4] Wilczek, F. & Zee, A. Appearance of gauge structure in simple dynamical systems. Phys. Rev. Lett. 52, 2111–2114 (1984).
- [5] Lloyd, S. Computation from geometry. Science 292, 1669 (2001).
- [6] Sjoqvist, E. *et al.* Non-adiabatic holonomic quantum computation. N. J. Phys. 14, 103035 (2012).
- [7] Johansson, M. *et al.* Robustness of non-adiabatic holonomic gates. Phys. Rev. A 86, 062322 (2012).
- [8] Jones, J. A., Vedral, V., Ekert, A. & Castagnoli, G. Geometric quantum computation using nuclear magnetic resonance. Nature 403, 869–871 (1999).
- [9] Feng, G., Xu, G. & Long G. Experimental Realization of Nonadiabatic Holonomic Quantum Computation. Phys. Rev. Lett. 110, 190501 (2013).
- [10] Nielsen, M. A. and Chuang, I. L. Quantum computation and quantum information. (Cambridge Univ. Press, 2010).
- [11] Duan, L. M., Cirac, J. I. & Zoller, P. Geometric manipulation of trapped ions for quantum computation. Science 292, 1695–1697 (2001).
- [12] Falci G. *et al.*, Detection of geometric phases in superconducting nanocircuits. Nature 407, 355–358 (2000).
- [13] Solinas, P., Zanardi, P., Zanghi, N. & Rossi, F. Holonomic quantum gates: a semiconductor-based implementation. Phys. Rev. A 67, 062315 (2003).
- [14] Abdumalikov, A. A. *et al.* Experimental realization of non-Abelian non-adiabatic geometric gates. Nature 496, 482 (2013).
- [15] Pfaff, W. *et al.* Unconditional quantum teleportation between distant solid-state quantum bits. Science 10.1126, 1253512 (2014).
- [16] Neumann, P. *et al.* Scalable quantum register based on coupled electron spins in a room temperature solid. Nature Physics 6, 249–253 (2010).
- [17] Yao, N. Y. *et al.* Scalable architecture for a room temperature solid-state quantum information processor. Nature Commun. 3, 800 (2012).
- [18] Dolde, F. *et al.* Room-temperature entanglement between single defect spins in diamond. Nature Physics 9, 139–143 (2013).
- [19] Dolde, F. *et al.* High-fidelity spin entanglement using optimal control. Nature Comm. 5, 3371 (2014).
- [20] Doherty, M. W. *et al.* The nitrogen-vacancy colour centre in diamond. Physics Reports 528, 1–45 (2013).
- [21] Shapere, A. & Wilczek F. Geometric phases in physics (World Scientific, Singapore, 1989).
- [22] Zhu, S. L. & Wang, Z. D. Implementation of universal quantum gates based on nonadiabatic geometric phases. Phys. Rev. Lett. 89, 097902 (2002).
- [23] Jacques, V. *et al.* Dynamic polarization of single nuclear spins by optical pumping of nitrogen-vacancy color centers in diamond at room temperature. Phys. Rev. Lett. 102, 057403 (2009).



- [24] Jelezko, F. *et al.* Observation of coherent oscillation of a single nuclear spin and realization of a two-qubit conditional quantum gate. *Phys. Rev. Lett.* 93, 130501 (2004).
- [25] White, A. G. *et al.* Measuring two-qubit gates. *J. Opt. Soc. Am. B*, 24, 172-183 (2007).
- [26] Yao, N. Y. *et al.* Robust quantum state transfer in random unpolarized spin chains. *Phys. Rev. Lett.* 106, 040505 (2011).
- [27] Jiang, L., Taylor, J. M., Sorensen, A. S. & Lukin, M. D. Distributed Quantum Computation Based-on Small Quantum Registers. *Phys. Rev. A* 76, 062323 (2007).
- [28] Duan, L. M. & Monroe, C. Quantum networks with trapped ions. *Rev. Mod. Phys.* 82, 1209 (2010).
- [29] Loredo, J. C., Broome, M. A., Smith, D. H., & White, A. G. Observation of Entanglement-Dependent Two-Particle Holonomic Phase. *Phys. Rev. Lett.* 112, 143603 (2014).
- [30] Pachos, J. K. Introduction to Topological Quantum Computation (Cambridge Univ. Press, 2012).

**Acknowledgements** We thank M. Lukin's group for helpful discussions. This work was supported by the National Basic Research Program of China 2011CBA00300 (2011CBA00302) and the quantum information project from the Ministry of Education of China. LMD acknowledges in addition support from the IARPA MUSIQ program, the AFOSR and the ARO MURI program.

**Author Contributions** L.M.D. conceived the experiment and supervised the project. C.Z., W.B.W., L.H., W.G.Z., C.Y.D., F.W. carried out the experiment. L.M.D. and C.Z. wrote the manuscript.

**Author Information** Reprints and permissions information is available at [www.nature.com/reprints](http://www.nature.com/reprints). The authors declare no competing financial interests. Correspondence and requests for materials should be addressed to L.M.D. (lmduan@umich.edu).

## METHODS

### Experimental setup

We use a home-built confocal microscopy, with an oil-immersed objective lens ( $N.A. = 1.49$ ), to address and detect single NV center in a type IIa single-crystal synthetic diamond sample (Element Six). A 532 nm diode laser, controlled by an acoustic optical modulator (AOM), is used for spin state initialization and detection. We collect fluorescence photons (wavelength ranging from 637 – 850 nm) into a single-mode fiber and detect them by the single-photon counting modular (SPCM), with a counting rate 105 kHz and a signal-to-noise ratio 15 : 1. The diamond sample is mounted on a 3-axis closed-loop Piezo for sub-micrometer resolution scanning. An impedance-matched gold coplanar waveguide (CPW) with 70  $\mu\text{m}$  gap, deposited on a cover-glass, is used for delivery of radio-frequency (RF) and microwave (MW) signals to the NV center.

In our experiment, we find a single NV center with a proximal  $C^{13}$  of 13.7 MHz hyperfine strength (Fig. 1). To polarize the nearby nuclear spins ( $C^{13}$  and the host  $N^{14}$ ), we apply a magnetic field of 451 G along the NV axis using a permanent magnet. Under this field, the electron spin levels  $|m = 0\rangle$  and  $|m = -1\rangle$  become almost degenerate in the optically excited state (called the esLAC, the electron spin level anti-crossing [23]), which facilitates electron-spin nuclear-spin flip-flop process during optical pumping. The spin flip-flop process leads to polarization of the nitrogen nuclear spin on the NV site and the nearby  $C^{13}$  nuclear spins after 2  $\mu\text{s}$  green laser illumination [23]. The Zeeman energy from the 451 G magnetic field shifts the energy difference between electron spin states  $|m = 0\rangle$  and  $|-1\rangle$  ( $|+1\rangle$ ) from the zero-field splitting 2870 MHz to 1601 MHz (4141 MHz) and the nuclear spin hyperfine splitting from 13.7 MHz to 14.15 MHz (13.25 MHz) for  $|-1\rangle$  ( $|+1\rangle$ ) levels. Due to the large splitting of  $m = \pm 1$  levels, we apply two independent MW sources (Rohde-Schwarz), locked by a 10 MHz reference Rubidium clock, to address each transition. To adjust the frequency and phase of the MW pulses, we mix each MW output with an AWG (Tektronix, 500 MHz sample rate). RF signals for nuclear spin manipulation are generated directly by another analog channel of the AWG. All the MW and RF signals are amplified by independent amplifiers, combined through a home-made circuit, and delivered to the CPW. The digital markers of the AWG are used to control the pulse sequence (including laser and SPCM) with a timing resolution of 2 ns.

For each experimental cycle, we start the sequence with 2  $\mu\text{s}$  laser illumination to polarize NV electron spin and nearby nuclear spins and end it with a 3  $\mu\text{s}$  laser pulse for spin state detection. We collect signal photons for 300 ns right after the detection laser rises, and another 300

ns for reference  $2\ \mu\text{s}$  later. With a photon collection rate of 105 kHz, we have an average of 0.03 photon counts per cycle. For measurement of each data, we repeat the experimental cycle at least  $10^6$  times, resulting in a total photon counts of  $3 \times 10^4$ . The error bars of our data account for the statistical error associated with the photon counting. To calculate the error bar of each data, we use Monte Carlo simulation by assuming a Poissonian distribution for the photon counts. For each simulation trial, we calculate the value of each data. Then, by sampling over all the trails according to the Poissonian distribution, we get statistics of the data (including its mean value and standard deviation, the error bar).

### Calibration of fluorescence levels for different states

Due to the esLAC that induces spin flip-flop during the detection and the imperfect initial polarization of the electron and nuclear spins, each spin component  $|m, m_n\rangle$  ( $m = 0, \pm 1$ ;  $m_n = \uparrow, \downarrow$ ) may fluorescent at different levels. Note that the spins are dominantly in the state  $|m = 0, m_n = \uparrow\rangle$  after the optical pumping. To calibrate the fluorescence level of each state, we therefore associate the detected fluorescence level right after the optical pumping with the state  $|m = 0, m_n = \uparrow\rangle$ . With MW or RF  $\pi$ -pulses (the  $\pi$ -pulses are calibrated through Rabi oscillations), we can make a complete transfer between  $|m = 0, m_n = \uparrow\rangle$  and any other  $|m, m_n\rangle$  spin component. For instance, with a  $\pi$ -pulse between  $|m = 0, m_n = \uparrow\rangle$  and  $|m = 0, m_n = \downarrow\rangle$  right after the optical pumping, we associate the detected fluorescence level with the

$|m = 0, m_n = \downarrow\rangle$  state. In this way, the characteristic fluorescence level of each component  $|m, m_n\rangle$  can be calibrated. With the calibrated fluorescence level for each spin component, we then read out the system state after the geometric gates through quantum state tomography [25].

### Quantum Process tomography

A quantum process can be described by a completely positive map  $\varepsilon$  acting on an arbitrary initial state  $\rho_i$ , transferring it to  $\rho_f \equiv \varepsilon(\rho_i)$ . In quantum process tomography (QPT), we choose a fixed set of basis operators  $\{E_m\}$  so that the map  $\varepsilon(\rho_i) = \sum_{mn} E_m \rho_i E_n^\dagger \chi_{mn}$  is identified with a process matrix  $\chi_{mn}$ . We experimentally measure this process matrix  $\chi$  through the maximum likelihood technique [25]. For single-bit QPT, we set the basis operators as  $I = I$ ,  $X = \sigma_x$ ,  $Y = -i\sigma_y$ ,  $Z = \sigma_z$  and choose four different initial states  $|0\rangle$ ,  $|1\rangle$ ,  $(|0\rangle + |1\rangle)/\sqrt{2}$ , and  $(|0\rangle - i|1\rangle)/\sqrt{2}$ . We reconstruct the corresponding final density operators through the standard quantum state tomography and use them to calculate the process matrix  $\chi_e$ . This process matrix  $\chi_e$  is compared with the ideal one  $\chi_{id}$  by calculating the process fidelity  $F_P = \text{Tr}(\chi_e \chi_{id})$ . The process fidelity  $F_P$  also determines the average gate fidelity  $\bar{F}$  by the formula  $\bar{F} = (dF_P + 1)/(d + 1)$  [25], where  $\bar{F}$  is defined as the fidelity averaged over all possible input states with equal weight and  $d$  is the dimension of the state space (with  $d = 2$  for a single qubit).